MORPHOLOGY-DIRECTED NANOSCOPIC ENERGY TRANSFERS IN PLASMONIC-ORGANIC HYBRIDS**

K. Gambhir [1,2], P. Sharma [1,2*], R. Mehrotra [1,2]

[1] Academy of Scientific & Innovative Research (AcSIR) at CSIR-National Physical Laboratory campus, New Delhi-110012, India, e-mail: sharmap2@nplindia.org
[2] Physico Mechanical Metrology Division, CSIR-National Physical Laboratory, Dr. K.S. Krishnan Marg, New Delhi-11012, India

We have experimentally realized a morphology-directed nanoscale energy transfer between an emitter, Eosin yellow dye, and three distinct gold nanoshapes, namely, nanospheres, nanopebbles, and nanoflowers. Raman spectroscopy is employed to ensure mutual interaction among the couple hybrids. The results explicitly show that plasmonic structures with sharp edges produce a strong localized electromagnetic field, which substantially suppresses the background fluorescence signals of the analyte. Further, the relationship between the observed quenching of the dye fluorescence and the geometrical factors of the gold nanoshapes is used to comprehend the influence of energy transfers on their enhanced third-order nonlinearity. The experimental findings reveal a relationship between the efficiency of energy transfers and the enhancement of the observed nonlinear optical coefficients. This study may act as the basis for designing active photonic nanocomposites based on their efficient energy transfer interactions.

Keywords: *gold nanostructures, fluorophores, nanoscopic energy transfer mechanisms, surface enhanced Raman scattering.*

МОРФОЛОГИЧЕСКИ НАПРАВЛЕННЫЙ НАНОСКОПИЧЕСКИЙ ПЕРЕНОС ЭНЕРГИИ В ПЛАЗМОННО-ОРГАНИЧЕСКИХ ГИБРИДАХ

K. Gambhir [1,2], P. Sharma [1,2*], R. Mehrotra [1,2]

УДК 535.375.5;620.3

[1] Академия научных и инновационных исследований (AcSIR) Национальной физической лаборатории CSIR, Нью-Дели 110012, Индия, e-mail: sharmap2@nplindia.org
[2] Отдел физико-механической метрологии Национальной физической лаборатории CSIR, Нью-Дели 110012, Индия

(Поступила 20 декабря 2019)

Реализован морфологически направляемый перенос энергии в наномасштабе между излучающим красителем эозином желтым и тремя различными наноформами золота — наносферами, наночастицами и наноцветами. Для подтверждения взаимодействия между связанными гибридными формами используется КР-спектроскопия. Установлено, что плазмонные структуры с острыми краями создают сильное локализованное электромагнитное поле, которое существенно подавляет фоновые сигналы флуоресценции аналита. Взаимосвязь между тушением флуоресценции красителя и геометрическими характеристиками наночастиц золота используется для понимания влияния передачи энергии на их усиленную нелинейность третьего порядка. Экспериментальные данные показывают взаимосвязь между эффективностью передачи энергии и увеличением нелинейно-оптических коэффициентов.

Ключевые слова: *наночастицы золота, флуорофор, наноскопический перенос энергии, поверхностно-усиленное комбинационное рассеяние.*

** Full text is published in JAS V. 88, No. 1 (http://springer.com/journal/10812) and in electronic version of ZhPS V. 88, No. 1 (http://www.elibrary.ru/title_about.asp?id=7318; sales@elibrary.ru).

Introduction. An essential requirement for realizing ultrafast photonic switches, optical limiters, and modulators is the substantial third-order optical nonlinearity of materials at considerably low light powers [1, 2]. However, most of natural materials possess insignificant nonlinearity in such a regime [3]. Therefore, the design and fabrication of nanoengineered materials with tunable absorption/emission spectra and considerable third-order optical nonlinearity, such as hybrid molecular-plasmonic nanostructures, are a topic of global research [4–6]. In particular, admixtures of fluorophore-plasmonic nanostructures have gained much interest due to flexibility in their design and versatile interaction mechanisms, which may further be fine-tuned to achieve the desired photonic characteristics [7, 8].

Plasmon-coupled fluorophores have led to substantial progress in high-throughput DNA detection [9, 10], bioimaging [11], drug delivery [12], photovoltaics [13], and light-emitting diodes [14]. On the other hand, the nonlinear optical fundamentals of such hybrid structures remain relatively unexplored compared to their linear counterparts. The interaction of a plasmonic structure with a fluorophore may either strengthen the local field felt by the organic molecule, thereby enhancing the optical emission/luminescence, or result in a strong damping of the luminescence of the fluorophore due to dipole and multipole interactions within the hybrid [15]. So far, the interaction studies of fluorophores with plasmonic structures have mainly focused on the electronic properties of metal nanostructures and the size and distance of separation between the fluorophore and the surface of the metal nanostructure [16, 17]. At the same time, the energy transfer, based dynamics of the photoinduced phenomenon within nanoconfined systems and its impact on the optical nonlinearity remain uninvestigated. The effect of dipolar interactions on the third-order nonlinear susceptibilities of various nanocomposites has been investigated using the coupled dipole method [18]. Moreover, it is important to note that the coupled dipole method is a linear approximation that must be employed only for weak optical fields [19, 20]. Furthermore, little attention has been paid to studying the effects of interparticle dipolar interactions within plasmonic organic hybrids. Recently, the unconventional idea of fluorescence resonance energy transfer (FRET) and nanometal-surface energy transfer (NSET) based hybrids offering giant enhancements in the optical nonlinearity has been proposed by Rakovich et al. [21] and Rosina Ho-Wu et al. [22], respectively. The same has been confirmed for thin films by Gambhir et al. [23].

FRET is a valuable method for the determination of submicroscopic separations among interactive molecules [24]. In this phenomenon, dipole-dipole interactions between the excited donor molecule (D) and the acceptor molecule (A) staying in the ground state result in a non-radiative exchange of energy between them. The length scale of nanoscopic FRET is restricted to 8 nm, beyond which it is too weak to be used as the energy transfer efficiency is inversely proportional to the sixth power of the distance between the donor and acceptor molecules [24, 25]. Recently, a long-range dipole-surface interaction mechanism based on NSET has been realized, whose range for energy transfer is twice as that for FRET [9]. Here, the rate of energy transfer from the oscillating dipole to the continuum of the electron-hole pair excitations in metal nanoparticles is inversely proportional to the fourth power of the donor-to-acceptor distance [25, 26]. In the linear regime, both these techniques are recognized as powerful tools for determining the distance in the donor-acceptor pair within a coupled hybrid [27, 28].

To better understand the influence of these energy transfers on third-order optical nonlinearity, we directed our research towards the factors affecting the third-order optical nonlinearity of plasmonic-organic hybrids. In our previous studies, we investigated the third-order nonlinearity in a technologically promising organic dye Eosin yellow (EY) hybridized with three distinct gold nanoshapes, namely, gold nanospheres (GNS), gold nanopebbles (GNP), and gold nanoflowers (GNF). It is demonstrated that these complexes underwent morphology-directed coupling between the localized plasmons of the metallic nanostructures and the H-aggregated molecular excitons. This phenomenon significantly improved the third-order nonlinear optical properties of the organic fluorophore. Indeed, up to a 120% increase in the nonlinear optical response of EY when adsorbed on GNF was demonstrated [29]. Further developing our prior study, in this paper, we report the influence of morphology-directed energy transfer on the third-order nonlinear optical properties of the synthesized plasmonic organic hybrids. Herein, the quenching of the fluorescence and lifetime of EY due to differently sized and structured gold nanoparticles was investigated using ultrafast optical pump-probe, UV/visible, and photoluminescence spectroscopy. Simultaneously, surface-enhanced Raman spectroscopy was conducted to confirm the mutual coupling between the plasmonic organic hybrids. The results reported herein revealed an interesting relationship between the efficiency of the energy transfer and the enhancement in the observed third-order optical nonlinear coefficients. These experimental outcomes may not only provide a way to deconvolute morphology-dependent complex third-order nonlinear optical interactions but are

also important in predicting the third-order optical nonlinearities of such hybrids based on their energy transfer phenomena.

Experimental. *Chemicals and reagents.* Hydrogen tetrachloroaurate(III) hydrate ($HAuCl_4 \cdot 3H_2O$), triethanolamine (TEA) [$(HOC_2H_4)_3N$] [$C_6H_{15}NO_3$], and ethylene glycol (EG) [$C_2H_6O_2$] were procured from Sigma Aldrich Chemicals, USA. Additionally, EY (Mol.Wt.-691.86) was purchased from Qualigens Fine Chemicals Division, Thermo Scientific Pvt. Ltd., India. Other analytical grade chemicals and reagents used in the experiments were utilized as received without any further purification. Deionized water obtained through a Milli Pore (Scholar-UV Nex UP 1000) water purification system was used for preparing aqueous stock solutions and their dilutions.

Sample preparation. Gold colloids were prepared using the Jiang *et al.* method with some modifications [30]. All three different nanoshapes were synthesized by changing the reaction solvent under the same experimental procedure; 200 μL of aqueous $HAuCl_4$ (1 wt %) solution was added to 20 mL of pure EG in a 60ºC water bath. Then 400 μL of freshly prepared TEA solution with a concentration of 2.5 M was added in four steps with mild stirring, and the reaction was allowed to run for 60 min. Gold nanoparticles were collected by centrifugation at 12000 rpm for 20 min, washed three times, redispersed in DI water, and utilized for different experiments. To study the effect on the final size and morphology of gold nanostructures, other solvents such as DI water and a mixture of ethylene glycol and DI water (1:1 (v/v)) were examined.

EY stock solution (5.78 mM) was prepared by dissolving 2 mg of dye in 500 μL of ethanol. The hybrids were prepared by the dropwise addition of different concentrations of EY to colloidal gold nanostructures. The eosin solution of a constant concentration (25 μM) and a 1:1 (v/v) ratio of EY with GNS, GNP, and GNF, respectively, was optimized for various spectroscopic investigations. An elaborate description of the optimization and characterization of gold nanostructures and their hybrids with EYis given elsewhere [29].

UV/visible spectroscopy. The extinction spectra of the films were collected using a Perkin Elmer Lambda-35 spectrophotometer. The UV/visible spectrophotometer was calibrated using a Normal Transmittance–Didymium Oxide filter (WC-DD-02c) traceable to the National Institute of Standards and Technology (NIST), USA, with a precision management of less than ±0.2 nm wavelength shift and ±0.5 absorbance variation. The spectral acquisitions were conducted in the scan range 400–700 nm.

Photoluminescence spectroscopy. Room temperature photoluminescence studies were recorded using an Edinburgh luminescence spectrometer (Model: F900) fitted with a xenon lamp with a slit width of 2 nm, and the spectral acquisitions were carried out in the scan range 300–700 nm.

Closed and open aperture Z-scan. The nonlinear optical properties of the gold nanostructures and their hybrids were investigated using the standard *Z*-scan technique. The experimental setup was comprised of a mode-locked Nd:YAG laser, frequency-doubled at 532 nm, characterized by a pulse duration of 20 ps with a repetition rate of 1 kHz and a 0.34 mJ pulse energy. The measured beam waist (ω_0) of the light source was 16±1 μm. A polarized Gaussian laser beam was focused using a 200 mm focal-length lens into the sample, placed in a 1 mm path length quartz cuvette. At each position, the sample experiences a different light intensity. The light intensities transmitted across the samples were measured as a function of the sample position in the *Z*-direction with respect to the focal plane, through a 0.5 mm aperture (closed aperture) and without aperture (open aperture). The on-axis transmitted beam energy, the reference beam energy, and their ratios were measured using silicon photodiodes and collected using a calibrated digital oscilloscope. The sample movement was performed using a translation stage. The setup was optimized using a standard CS_2 solution. The eosin solution of a constant concentration (100 μM) was optimized. Three different molar ratios (*r*) 1:1, 1:2, 1:4 of EY were prepared with gold nanoparticles for nonlinear optical studies. The sample was shaken between the measurements to ensure the homogeneity of the solution.

Raman spectroscopy. The dye solution and the gold colloidal solution at a 1:1 (v/v) ratio were pipetted onto a glass microscope slide and allowed to dry; after that, a Renishaw in Via Raman microscope combined with an epi-illuminated Leica microscope having a 1 cm^{-1} axial resolution was employed for Raman Spectroscopic investigations. The spectral acquisition was conducted using a 785 nm laser source with a 2.5 mW power and a 40 s exposure time. A holographic grating with 1200 grooves/mm was used with a 3 cm^{-1} resolution. The spectra were gathered using an Olympus microscope equipped with a 50× long working distance objective lens. Thereafter, WIRE 3.4 software was used to analyze the observed Raman spectra. The scan range 600–1700 cm^{-1} was used for all the samples. All the samples were scanned thrice to ensure reproducibility.

Ultrafast transient absorption spectroscopy. Ultrafast time-resolved pump-probe spectroscopy (UTRPPS) was employed for the lifetime measurement of the samples. A beam splitter was used to split the train of an optical pulse from a Ti:sapphire laser (35 fs, 4 mJ/pulse, 1 kHz, 800 nm) into two beams. The

beam with a higher intensity was employed as a pump, and an optical parametric amplifier (TOPAS, Light Conversion) was used to vary the wavelength of this pump beam from 190 to 2600 nm. For all the experiments reported herein, a 410 nm pump beam at normal incidence was employed. The beam with a weaker intensity, i.e., the probe, was passed through a CaF_2 crystal to generate a white-light continuum (WLC) covering the whole spectrum of the visible light to be used as a probe beam. Thereafter, the probe was optically delayed with respect to the pump beam using a controlled delay stage, having an intrinsic temporal resolution of 7 fs. Meanwhile, the changes in the absorption spectra were detected using a gated CMOS detector. The time-resolved study was performed using a HELIOS (Ultrafast systems) spectrometer.

Results and discussion. *Raman spectroscopic analysis of EY on differently shaped gold nanostructures.* Raman spectroscopy of the free-form colloidal EY dye (100 μM) dissolved in DI water with respect to the hybridized EY-GNP, EY-GNS, and EY-GNF (1:1 (v/v)) was performed to confirm the mutual interaction between the coupled hybrids (Fig. 1). As depicted in Fig. 1. the conjugation of EY with various nanoshapes leads to a shift in the wavenumber of several bands, such as υ(C-C) stretching band shifts from 1469, 1495, and 1564 cm^{-1} to 1481, 1504, and 1572 cm^{-1}, respectively, which indicates significant mutual interaction between the organic molecules and the plasmonic structures [31]. It is well known that the enhancement observed in the Raman spectrum is mainly due to electromagnetic (EM) and chemical interactions. The interaction of the electric field of the surface plasmons with the transition moment of the adsorbed molecule causes EM enhancement, whereas mixing the metal orbitals with the orbitals of the molecule leads to a chemical mechanism, which also facilitates charge transfer among the conjugates [32]. Further, Lombardi et al. [32] proposed a charge transfer model according to which only totally symmetric vibrational modes of the probe molecules get enhanced via the Franck−Condon contribution, whereas, the Herzberg–Teller effect leads to the enhancement of both the totally and non-totally symmetric vibrational bands of the probe molecule. They also concluded that the b_2 modes (in-plane, out-of-phase modes) are selectively enhanced by the CT mechanism through the Herzberg–Teller contribution, while the a_1 modes (in-plane, in-phase modes) depict the EM contribution in the SERS spectrum.

In-phase modes, or symmetric stretching, is where the bonds of a molecule stretch and contract in phase with each other and are symmetric with respect to the principal axis of the symmetry, whereas antisymmetric stretch, or out-of-phase modes, are the ones where bonds of the molecule vibrate out of phase with each other, i.e., one bond contracts as the other stretches and thus are antisymmetric with respect to the principal axis of the symmetry [33]. Since these modes represent a characteristic frequency; they are useful in determining the molecular structure, dynamics, and environment of the sample.

The Raman spectra of various EY hybrids (Fig. 2) predominantly demonstrate in-plane, in-phase modes, such as υ(CC), υ(CH), and υ(C-Br) at 649, 1063, and 771 cm^{-1}, respectively [34]. The prevalence of such bands in a SERS spectrum indicates that the observed enhancement may be due to an electromagnetic (EM) mechanism. Meanwhile, the enhancement of in-plane, out-of-phase modes observed at 715, 1181, and 1286 cm^{-1} is also visible, which may be attributed to efficient charge transfer between the metal and the adsorbed dye molecules [32].

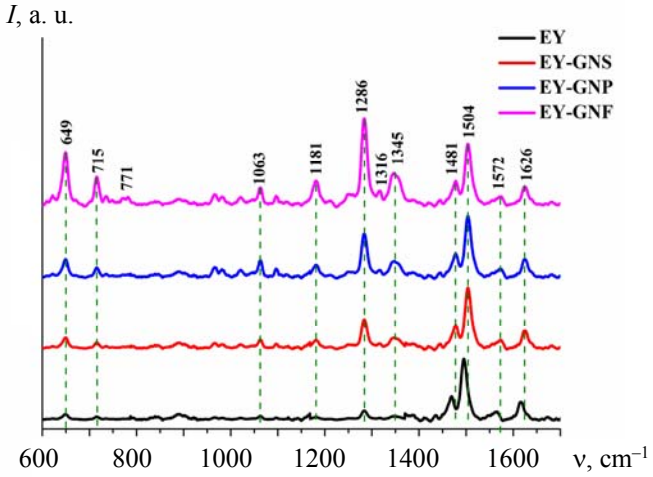

Fig. 1. Stack view of the Raman spectra of free EY and its hybrids plotted on the same intensity scale.

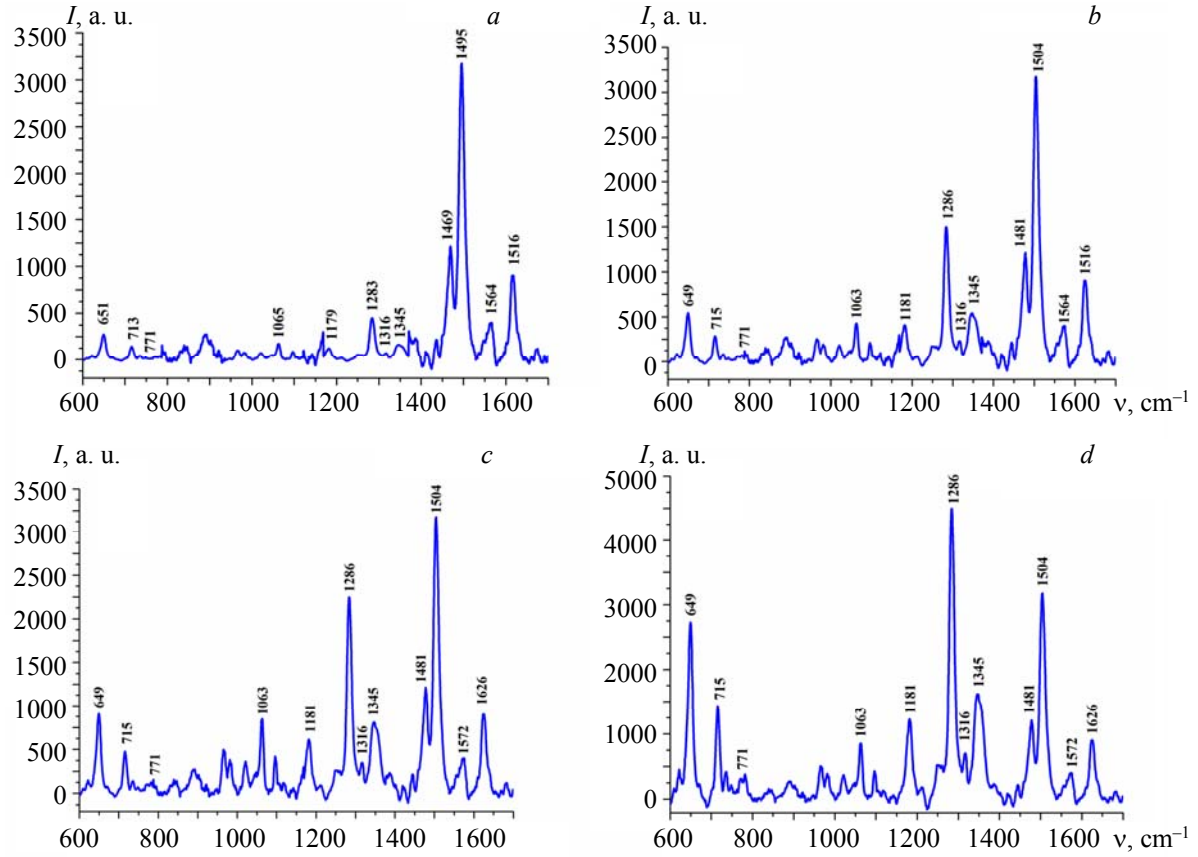

Fig. 2. Raman spectra of (a) colloidal EY, (b) colloidal EY-GNS hybrid, (c) colloidal EY-GNP hybrid, and (d) colloidal EY-GNF hybrid.

Further, the intensity of Raman peaks depends on various factors such as concentration differences, molecular orientation differences, morphological differences, aggregate formation, and so on [35, 36]. In the discussed samples, apart from the reported morphological differences in the gold nanoshapes, all other experimental conditions were kept constant for the discussed hybrids (optimized using absorbance spectroscopy [29]). Therefore, the authors claim that the substantial variation observed in the SERS spectra may be attributed to the shape-dependent interaction of gold nanoparticles with the dye molecules (Figs. 1 and 2). The presence of various sharp petals in the GNF structure with distinct lengths and random orientations might have led to a greater surface area, and a larger number of hotspots in context to GNS and GNP are observed. TEM micrographs and HR-TEM images of the synthesized gold nanostructures are given elsewhere [29].

The observed enhancement of the various bands in the SERS signal is different for each morphology and follows the order of nanoflowers > nanopebbles > nanospheres. The results infer that the nanostructures with sharp edges offer plenty of hotspots and may be candidates for highly sensitive SERS probes.

One of the major limitations in attaining the Raman spectra of fluorescent organic compounds is the presence of a prominent fluorescence background (FB), which totally/partially obscures the signal [37]. Hence, prominent fluorescence noise is observed in the Raman signal of the free EY, collected using an excitation wavelength of 785 nm. Various complex approaches such as the polarization-difference technique [38], femtosecond stimulated Raman spectroscopy [39], and high-performance picosecond Kerr gate [40] were adopted to eliminate the fluorescence noise. The results depicted herein provide a simple and effective Raman analysis of fluorescent samples when conjugated with plasmonic structures with sharp edges.

Nonlinear optical properties. *Z*-scan spectroscopy is regarded as the standard technique for determining the third-order nonlinear optical (NLO) coefficients due to its high sensitivity and simple instrumentation [41]. This technique involves focusing a Gaussian beam onto the sample, which leads to alteration in the energy distribution. Translation of the sample along the *Z*-direction causes a change in the refractive index and the absorption coefficient as a function of intensity in the far-field. This variation in the intensity is recorded along with the sample position and theoretically fitted for calculating the third-order NLO coefficients.

The nonlinear absorption coefficient (β) was calculated by fitting the experimental data using the equation described by Sheik-Bahae et al. [42].

The expression for the normalized transmittance of an open aperture *Z*-scan is as follows:

$$T_{OA(2PA)} = 1 - \frac{\beta I_0 L_{EFF}}{2^{3/2}(1 + z^2 / z_0^2)}, \quad (1)$$

where z is the sample position, $z_0 = \pi\omega_0^2/\lambda$ is the Rayleigh range, ω_0 is the beam waist at focus, λ is the wavelength, I_0 is the peak intensity, calculated to be 2.11 TW/cm^2 while the calculated fluence is 0.423 J/cm^2, and β denotes the nonlinear absorption coefficient. The effective optical path length is defined as

$$L_{EFF} = (1 - e^{-\alpha_0 L})/\alpha_0, \quad (2)$$

where α_0 is the linear absorption coefficient and L is the sample length (1 mm).

Measurements of the nonlinear refractive index (n_2) for the gold nanoparticles, as well as their hybrids, were performed by the closed aperture *Z*-scan technique. The theoretical fit of the experimental data was performed using the equation

$$T_X = 1 - \frac{4X\Delta\phi_0}{(X^2 + 9)(X^2 + 1)}. \quad (3)$$

Here, T is the normalized transmittance for closed aperture, $X = z/z_0$, $\Delta\phi_0 = kn_2I_0L_{EFF}$ is the on-axis nonlinear shift at the focus, and k is the wavenumber.

The experimental data obtained for gold nanoparticles, dye EY, and its hybrids using *Z*-scan spectroscopy, its theoretical fitting, and calculations have already been published elsewhere [23, 29]. Table 1 enlists the nonlinear optical coefficients of all four gold nanostructures, EY, and its hybrids.

TABLE 1. Two-photon Absorption Coefficients of EY, Plasmonic Nanoshapes, and Their Hybrids

Samples	Nonlinear absorption coefficient β, cm/GW	Nonlinear refractive index $n_2\times10^{-15}$, cm^2/W
EY	0.475±0.021	3.508±0.983
GNF	0.365±0.014	2.66±0.654
GNP	0.111±0.038	0.820±0.023
GNS	0.268±0.015	1.976±0.270
EY-GNF	1.058±0.041	7.807±0.618
EY-GNP	0.664±0.037	4.901±0.541
EY-GNS	0.631±0.069	4.605±0.385

Morphology-directed energy transfer. In general, the plasmon resonance absorption band of gold nanoparticles is in the 400–800 nm wavelength region of the electromagnetic spectrum [43], whereas it has been experimentally demonstrated that the plasmon resonance wavelengths of gold nanoparticles can be varied from blue to infrared wavelengths by modifying the morphology of the nanoparticles [44]. Figure 3 shows that the extinction spectra of GNF, GNP, and GNS nanostructures exhibit absorption peaks at 581, 529, and 531 nm, respectively. Since the average size of GNF was reported to be 55 nm, those of GNS and GNP were determined to be 30 and 34 nm, respectively [45].

Hence, the observed spectra are in accordance with the correlation between the morphology and extinction spectra of the metallic nanoshapes. A clear spectral overlap was observed between the emission spectra in terms of the PL intensity of the donor fluorescent dye (centered at 544 nm) and the absorption spectra of acceptor GNF, GNP, and GNS, meeting the necessary condition for the energy transfer to take place [13]

Further, the dye EY was hybridized with GNP, GNF, and GNS at a fixed ratio 1:1 (v/v) to study the impact of the gold nanostructures on the energy transfer mechanism. Figure 4a illustrates a drastic quenching effect in the PL intensity, i.e., 30, 55, and 67% when hybridized with GNS, GNP, and GNF, respectively, accompanied by a hypsochromic shift in the emission spectra in terms of the PL intensity of the dye. The observed quenching in the emission spectra in terms of the PL intensity is extremely sensitive to the morphology-directed plasmon coupling effect, which originated from the space interaction between the free electrons of metal nanoparticles and the dipoles of the dye molecules [24].

To decipher the cause of the quenching, the radiative rate (k_r) was calculated using the equation

$$k_r = 3.13\times10^{-9}\,\nu_0^2 \int \varepsilon d\bar{\nu} \cong \nu_0^2 f, \quad (4)$$

where ν_0 is the maximum absorption energy of the dye in the wavenumber, ε is the extinction coefficient, and *f* denotes the oscillator strength of the eosin molecules. The calculated radiative rates are 1.50×10^7 s^{-1} for the dye and 1.40×10^7, 1.43×10^7, and 1.45×10^7 s^{-1} for EY-GNF, EY-GNP, and EY-GNS hybrids, respectively. The variation in the oscillator strength is estimated to be 3–7%, which is nominal in comparison to the quenching of the PL intensity. This implies that the quenching process is due to a non-radiative energy transfer process [13].

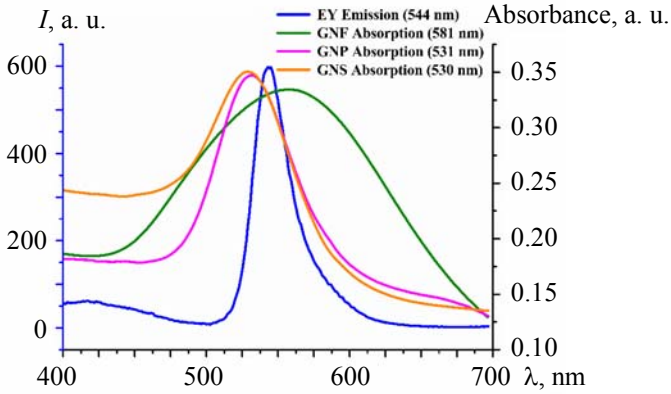

Fig. 3. Absorption spectra of Au nanoshapes and emission spectra in terms of the PL intensity of free EY.

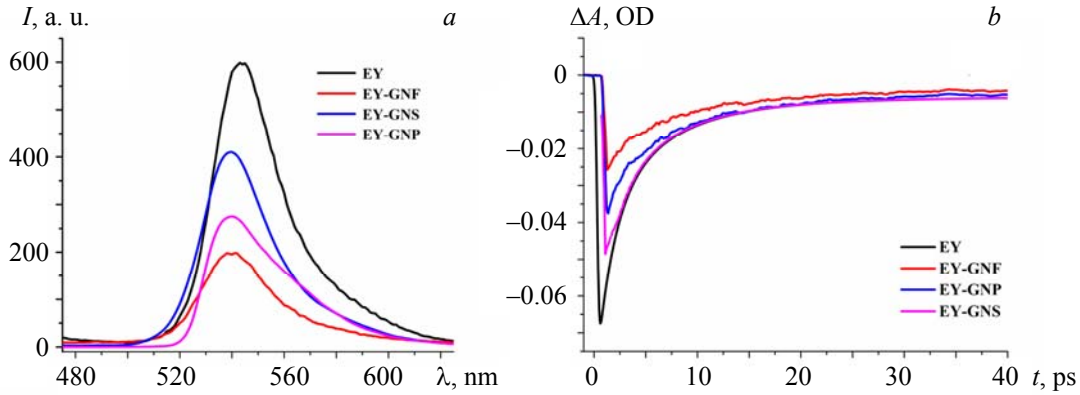

Fig. 4. a) Emission spectra in terms of the PL intensity of free EY and its hybrids; b) decay curves of free EY and its hybrids (pump wavelength: 410 nm; pump intensity: 1.5 mW).

Ultrafast time-resolved pump-probe spectroscopy was employed to obtain the decay lifetimes of the EY, gold nanostructures, and its hybrids. The decay lifetimes of colloidal EY and its hybrids were fitted to one or more lifetime components by linearizing the fitting function according to the Marquardt algorithm [46]. Satisfactory fits were judged by examination of the fitted decay, the weighted residuals, the autocorrelation of the residuals, and the reduced chi-square values.

The function to describe the intensity of the decay curve is $I(t) = \sum_{i=1}^{n} A_i e^{-t/\tau_i}$. The following tri-exponential fitting equation is used:

$$S(t) = e^{-\left(\frac{t-t_0}{IRF}\right)} \left\{ A_1 e^{-\left(\frac{t-t_0}{\tau_1}\right)^2} + A_2 e^{-\left(\frac{t-t_0}{\tau_2}\right)^2} + A_3 e^{-\left(\frac{t-t_0}{\tau_3}\right)^2} \right\},$$

the mean (intensity weighted) lifetime is given by the equation

$$\tau_{av} = \sum_{i=1}^{n} A_i \tau_i^2 \Big/ \sum_{i=1}^{n} A_i \tau_i , \quad (5)$$

where IRF is the instrument response function, t_0 is time zero, τ_i and A_i are the individual decay time and carrier population, and $n = 3$; τ_{av} determines the average lifetime a molecule spends in an excited state. During the fit, the A_i and τ_i parameters were not constrained and were iteratively adjusted until convergence was achieved according to acceptably small changes in each parameter.

Conventionally, plasmons in metal nanoparticles are expected to undergo a three-step relaxation process, which includes electron-electron scattering and plasmon dephasing in the femtosecond regime; 10–100 ps timescale is attributed to electron-phonon energy dissipation, and a slower, >100 ps, effect signifies the transfer of energy to the adjacent environment [47, 48]. The coupling time observed in our experimental investigations falls in the *e*-ph coupling domain for all the discussed gold nanoshapes. Furthermore, Fig. 4b shows that the average lifetime at 536 nm of the donor dye (τ_{av}) quenches from 70.68 ps to 58.45, 50.62, and 47.82 ps when hybridized with GNS, GNP, and GNF, respectively; it may be inferred that on hybridizing these nanoshapes with the EY dye, EY-gold nanohybrids absorb at 410 nm, and EY transfers its energy internally within the EY-GNX hybrid.

Table 2 depicts the tri-exponential decay lifetimes observed for both isolated EY and EY hybrids. The significant reduction in the fast decay time (τ_1) of the hybrids may be attributed to a decrease in the radiative rate due to the coupling between dye molecules and plasmonic gold nanoshapes, which led to a robust chromophore-metal resonance energy transfer process. The intermediate decay time (τ_2) may be associated with non-radiative energy transfer interactions, which might occur due to direct coupling between excitons of dye molecules and indirect coupling of dye excitons via gold plasmons. Meanwhile, the longest emission decay kinetics (τ_3) may be due to those dye molecules that could not overcome coupling effects, being far away from the metal nanoshapes [49].

TABLE 2. Decay Time Constants for Free form EY and EY Hybrids as Derived by Fitting the Kinetic Traces into a Tri-Exponential Model Function

Sample	100 μM Colloidal EY	EY-GNS	EY-GNP	EY-GNF
A_1	–0.611	–0.541	–0.786	–0.587
τ_1, ps	11.21	4.34	5.86	8.35
A_2	–0.285	–0.323	0.166	–0.373
τ_2, ps	25.68	12.6	17.4	13.49
A_3	–0.103	–0.135	–0.048	–0.039
τ_3, ps	127	85.6	108.6	123.9
Average, ps	70.68	58.45	50.62	47.82

The energy transfer efficiency (Φ_{ET}) from dye to gold nano shapes is calculated using the equation

$$\Phi_{ET} = 1 - (\tau_{DA}/\tau_D), \quad (6)$$

where τ_{DA} and τ_D are the decay time of the hybrid and the dye, respectively. The estimated energy transfer efficiency from dye to GNS, GNP, and GNF is determined as 17.31, 28.39, and 32.35%, respectively.

The Förster distance (R_0) is calculated as

$$R_0 = 0.211[k^2 n^{-4} \Phi_{dye} J(\lambda)]^{1/6} \text{ Å}, \quad (7)$$

where k^2 depicts the orientation factor, Φ_{dye} is the quantum efficiency of the dye, n is the refractive index of the medium, and $J(\lambda)$ is the overlap integral between the absorption peak of gold nanoshapes and the emission peak of the dye, as seen in Figs. 5–7a.

The overlap integral $J(\lambda)$ was obtained using the numerical integration method from the equation

$$J(\lambda) = \frac{\int_0^\infty F(\lambda)\varepsilon_A(\lambda)d\lambda}{\int_0^\infty F(\lambda)d\lambda}, \quad (8)$$

where $F(\lambda)$ depicts the normalized total fluorescence intensity of the donor in the λ to $(\lambda + \Delta\lambda)$ wavelength range, and $\varepsilon_A(\lambda)$ is attributed to the acceptor's molar extinction coefficient at wavelength λ in $\text{mol}^{-1} \cdot \text{dm}^3 \cdot \text{cm}^{-1}$. From Eq. (7), the corresponding R_0 is calculated using $k^2 = 2/3$, $n = 1.4$, $\phi_{dye} = 0.93$,

and $J(\lambda) = 3.671\times10^{15}$ for EY-GNS, 5.187×10^{15} for EY-GNP, and $7.314 \cdot 10^{16}\,M^{-1} \cdot cm^{-1} \cdot nm^4$ for EY-GNF. The calculated Förster distance (R_0) is 57.1, 60.5, and 92.1 Å for EY-GNS, EY-GNP, and EY-GNF, respectively, while the distance (d) between donor and acceptor is 74.2, 69.5, and 112 Å, respectively.

In general, the quantum efficiency of the energy transfer can be written as given

$$\phi_{ET} = \frac{1}{1+(d/R_0)^{n^*}}, \tag{9}$$

where n^* is the fitting parameter.

The energy transfer efficiency in the FRET mechanism is inversely proportional to the sixth power of the spatial distance between the donor and acceptor molecules; thereby, $n^* = 6$. Figures 5–7 represent a plot of the comparison between the theoretical curve attained using Eq. (9) and experimental data of the same sample. The average value of n^* is obtained as 6, and R_0 as 66.2 and 61.7 Å for EY-GNS and EY-GNP, respectively. It has been well studied that the length scale for FRET-based detection is confined only to a distance of 80 Å [50]. Beyond this limit, the energy transfer becomes extremely weak. Therefore, for EY-GNF, following the NSET model, the average values of n^* were kept as 4 and R_0 as 92.1 Å.

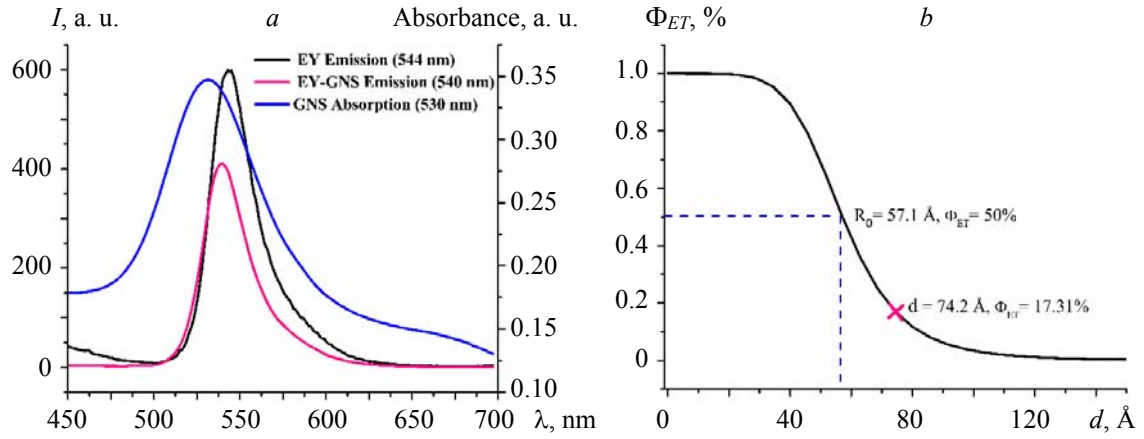

Fig. 5. a) D-A energy transfer pair along with the resultant emission spectra in terms of the PL intensity of EY-GNS; b) Theoretical plot of the energy transfer efficiency versus the separation distance between the dye and GNS, where d is the experimentally calculated distance for the EY-GNS hybrid.

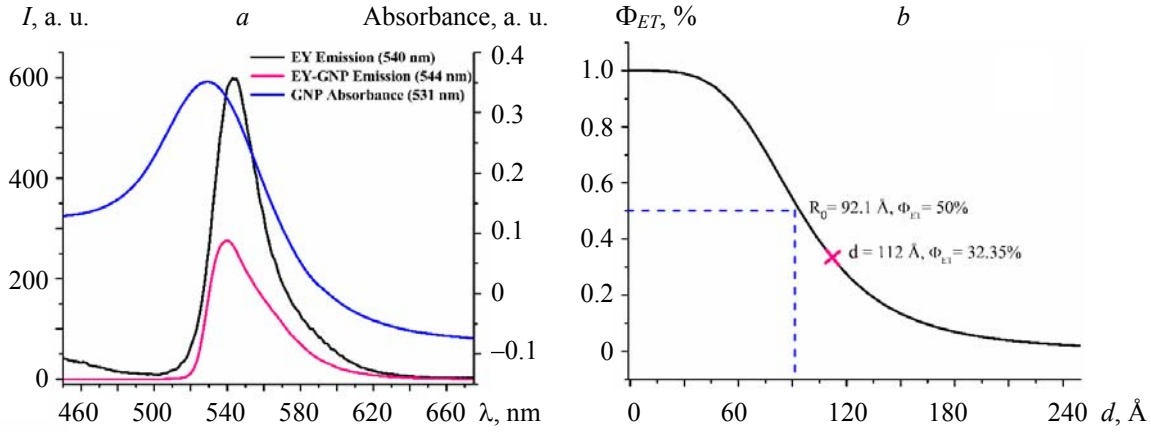

Fig. 6. a) D-A energy transfer pair along with the resultant emission spectra in terms of the PL intensity of EY-GNP; b) Theoretical plot of the energy transfer efficiency versus the separation distance between the dye and GNP, where d is the experimentally calculated distance for the EY-GNP hybrid.

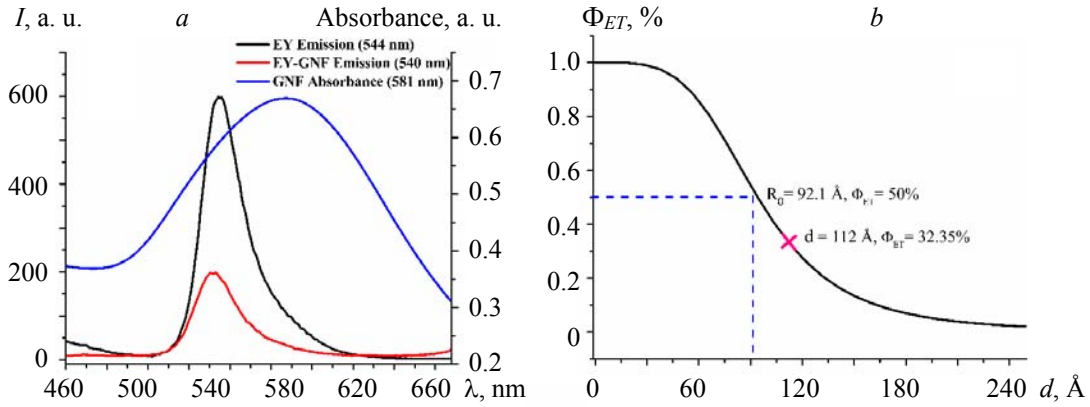

Fig. 7. (a) D-A energy transfer pair along with the resultant emission spectra in terms of the PL intensity of EY-GNF; b) Theoretical plot of the energy transfer efficiency versus the separation distance between the dye and GNF, where *d* is the experimentally calculated distance for the EY-GNF hybrid.

We also calculated the R_0 value of EY-GNF hybrid by using the Persson model [51, 52]:

$$R_0 = \left(\frac{0.525 c^3 \Phi_D}{\omega_D^2 \omega_F k_F} \right)^{1/4}, \quad (10)$$

where c symbolizes the speed of light in m/sec, $\Phi_D = 0.93$ denotes the quantum yield of the free donor molecule, ω_D and ω_F are the angular frequency of the donor molecule (3.6×10^{15} s^{-1}) and that of bulk gold (8.4×10^{15} s^{-1}), respectively, and k_F depicts the Fermi wave vector for bulk gold (1.2×10^{8} cm^{-1}) [50]. The calculated R_0 came out to be 89 Å, which is in close proximity with the average value estimated through the NSET model (i.e., 87 Å). The simulated curve uses $n = 4$, and this value of R_0 is shown in Fig.7b, which implies the operating mechanism is NSET and not FRET for the EY-GNF hybrid. Hence, it may be inferred that the fluorescence quenching phenomenon is size-sensitive since the results explicitly show that larger gold nanostructures (GNF ~55 nm) efficiently influenced the fluorescence of EY from a greater distance (92.1 Å).

Altogether, gold nanospheres, nanopebbles, nanoflowers, and their hybrids cannot be absolutely compared due to various complex factors involved, such as the coverage area of the dye, orientation, the precise surface area of the nanostructures available, the particle size distribution, and so on [53]. Nevertheless, based on the above outcomes and our past third-order nonlinearity results [29], it can be safely inferred that EY and gold nanoshapes form an efficiently interacting system.

Although a well-developed discussion is required to conclude the existence of a relationship between third-order nonlinearity and nanoscopic energy transfers, this is a relatively new direction. Rakovich et al. [21] and Rosina Ho-Wu et al. [22] proposed giant enhancements in the optical nonlinearity in Forster resonance energy transfer (FRET) and nanometal-surface energy transfer (NSET) based hybrids respectively. The same has been confirmed for plasmonic-organic thin films by Gambhir et al. [23]. Therefore, the previously reported enhancement in the third-order nonlinear coefficients may be attributed to the underlying energy transfer mechanisms associated with these hybrids. While there are undoubtedly other interactions present, such as morphology-directed aggregation of the dye onto the nanoparticles and formation of hotspots as discussed previously, the role of the energy transfer appears to be dominant as it is interesting to note that the enhancement is directly proportional to the calculated efficiency of the charge transfer (Table 3).

TABLE 3. Spectroscopic and Transient Kinetic Analysis of EY when Hybridized with GNS, GNP, and GNF

Hybrid	PL quenching, %	Lifetime quenching (EY = 70.68 ps), ps	Distance between D-A pair, Å	Förster distance, Å	Energy transfer efficiency, %	Energy transfer mechanism	Enhancement in TPA coefficients, %
EY-GNS	30	58.45	74.2	57.1	17.31	FRET	32
EY-GNP	55	50.62	69.5	60.5	28.39	FRET	39
EY-GNF	67	47.82	112	92.1	32.35	NSET	12

Conclusions. Hybrids of distinct gold nanoshapes with an organic fluorophore (Eosin yellow) have been used to systematically study morphology-directed energy transfer through photoluminescence, Raman, and UV/visible spectroscopy. Further energy transfer-based improvement in the Raman-to-fluorescence ratio were also reported in this paper. The results show that there is morphology-directed suppression in the fluorescence background when excited with a 785 nm laser wavelength, and they are in the following order: nanoflowers > nanopebbles > nanospheres. It is inferred from the study that the energy transfer within the EY-GNF hybrid was NSET, while, in conjugation with GNS and GNP, FRET dominated the interaction. The results indicate an exciting relationship between the efficiency of the energy transfer mechanism and the enhancement in the third-order nonlinear coefficients. These results may provide a new paradigm for designing hybrid systems offering significant nonlinear interactions at low light powers. Further, the absorption of energy by gold nanoparticles in such energy transfer-based nanohybrids may also find potential applications in gold-based photoredox reactions [54–56]. A crucial link-up of these results would be the study of the transient absorption dynamics of EY hybrids, where the possibility of coupling between the various electronic states of the metallic nanostructures and the dye may be explored. These results may also indicate the dark states involved in the EY photocycle, which come into the play due to plausible coupling with the plasmonic resonances.

Acknowledgments. The authors are thankful to the Director and the Divisional Review Committee, CSIR-National Physical Laboratory, New Delhi-110012, for granting permission to publish this work. Kaweri Gambhir acknowledges financial support from the Council of Scientific & Industrial Research, India.

REFERENCES

1. N. T. Fofang, N. K. Grady, Z. Fan, A. O. Govorov, N. J. Halas, *Nano Lett.*, **11**, No. 4, 1556–1560 (2011).
2. M. R. Shcherbakov, P. P. Vabishchevich, A. S. Shorokhov, K. E. Chong, D.-Y. Choi, I. Staude, A. E. Miroshnichenko, D. N. Neshev, A. A. Fedyanin, Y. S. Kivshar, *Nano Lett.*, **15**, No. 10, 6985–6990 (2015).
3. D. E. Chang, V. Vuletić, M. D. Lukin, *Nature Photonics*, **8**, No. 9, 685–694 (2014).
4. S.-J. Ding, F. Nan, D.-J. Yang, X.-L. Liu, Y.-L. Wang, L. Zhou, Z.-H. Hao, Q.-Q. Wang, *Sci. Rep*., **5**, 9735–9748 (2015).
5. M. Kucherenko, V. Stepanov, N. Y. Kruchinin, *Opt. Spectrosc*., **118**, No. 1, 103–110 (2015).
6. A. J. Wilson, K. A. Willets, *Ann. Rev. Anal. Chem*., **9**, No. 1, 27–43 (2016).
7. T. Ming, L. Zhao, H. Chen, K. C. Woo, J. Wang, H.-Q. Lin, *Nano Lett.*, **11**, No. 6, 2296–2303 (2011).
8. C. Tserkezis, N. Stefanou, M. Wubs, N. A. Mortensen, *Nanoscale*, **8**, No. 40, 17532–17541 (2016).
9. C. J. Breshike, R. A. Riskowski, G. F. Strouse, *J. Phys. Chem. C*, **117**, No. 45, 23942–23949 (2013).
10. J.-F. Li, C.-Y. Li, R. F. Aroca, *Chem. Soc. Rev*., **46**, No. 13, 3962–3979 (2017).
11. S.-J. Ding, F. Nan, X.-L. Liu, Z.-H. Hao, L. Zhou, J. Zeng, H.-X. Xu, W. Zhang, Q.-Q. Wang, *Sci. Rep*., **7**, No. 7, 43282–43289 (2017).
12. T. L. Doane, C. Burda, *Chem. Soc. Rev*., **41**, No. 7, 2885–2911 (2012).
13. F. Nan, S.-J. Ding, L. Ma, Z.-Q. Cheng, Y.-T. Zhong, Y.-F. Zhang, Y.-H. Qiu, X. Li, L. Zhou, Q.-Q. Wang, *Nanoscale*, **8**, No. 32, 15071–15078 (2016).
14. K. Okamoto, M. Funato, Y. Kawakami, K. Tamada, *J. Photochem. Photobiol. C: Photochem. Rev*., **32**, 58–77 (2017).
15. N. Hoa, C. Ha, D. Nga, N. Lan, T. Nhung, N. Viet, *J. Phys.: Conf. Ser.* IOP Publ. (2016) 012009.
16. H. Chen, T. Ming, L. Zhao, F. Wang, L.-D. Sun, J. Wang, C.-H. Yan, *Nano Today*, **5**, No. 5, 494–505 (2010).
17. E. Cao, W. Lin, M. Sun, W. Liang, Y. Song, *Nanophotonics*, **7**, No. 1, 145–167 (2018).
18. A. V. Panov, *J. Mod. Opt*., **60**, No. 11, 915–919 (2013).
19. M. A. Yurkin, A. A. Hoekstra, *J. Quant. Spectrosc. Radiat. Transfer*, **171**, 82–83 (2016).
20. M. A. Yurkin, A. G. Hoekstra, *J. Quant. Spectrosc. Radiat. Transfer*, **112**, No. 13, 2234–2247 (2011).
21. A. Rakovich, I. Nabiev, A. Sukhanova, V. Lesnyak, N. Gaponik, Y. P. Rakovich, J. F. Donegan, *ACS Nano*, **7**, No. 3, 2154–2160 (2013).
22. R. Ho-Wu, S. H. Yau, T. Goodson III, *ACS Nano*, **10**, No. 1, 562–572 (2016).
23. K. Gambhir, P. Sharma, A. Sharma, S. Husale, R. Mehrotra, *Dyes Pigments*, **155**, 313–322 (2018).
24. T. Sen, A. Patra, *J. Phys. Chem. C*, **116**, No. 33, 17307–17317 (2012).
25. P. C. Ray, Z. Fan, R. A. Crouch, S. S. Sinha, A. Pramanik, *Chem. Soc. Rev*., **43**, No. 17, 6370–6404 (2014).
26. S. Rakshit, S. P. Moulik, S. C. Bhattacharya, *J. Colloid Interface Sci*., **491**, 349–357 (2017).

27. H. Sahoo, *J. Photochem. Photobiol. C: Photochem. Rev.*, **12**, No. 1, 20–30 (2011).
28. E. Oh, A. L. Huston, A. Shabaev, A. Efros, M. Currie, K. Susumu, K. Bussmann, R. Goswami, F. K. Fatemi, I. L. Medintz, *Sci. Rep*., **6**, 35538–35547 (2016).
29. K. Gambhir, B. Ray, R. Mehrotra, P. Sharma, *Opt. Laser Technol*., **90**, 201–210 (2017).
30. Y. Jiang, X.-J. Wu, Q. Li, J. Li, D. Xu, *Nanotechnology*, **22**, No. 38, 385601–385611 (2011).
31. N. G. Greeneltch, A. S. Davis, N. A. Valley, F. Casadio, G. C. Schatz, R. P. Van Duyne, N. C. Shah, *J. Phys. Chem. A*, **116**, No. 48, 11863–11869 (2012).
32. J. R. Lombardi, R. L. Birke, *J. Phys. Chem. C*, **112**, No. 14, 5605–5617 (2008).
33. P. Larkin, *Infrared and Raman Spectroscopy: Principles and Spectral Interpretation*, Elsevier (2017).
34. V. A. Narayanan, D. L. Stokes, T. Vo-Dinh, *J. Raman Spectrosc*., **25**, No. 6, 415–422 (1994).
35. T. Wang, X. Hu, S. Dong, *J. Phys. Chem. B*, **110**, No. 34, 16930–16936 (2006).
36. F. Shan, X.-Y. Zhang, X.-C. Fu, L.-J. Zhang, D. Su, S.-J. Wang, J.-Y. Wu, T. Zhang, *Sci. Rep*., **7**, No. 1, 6813–6820 (2017).
37. D. Wei, S. Chen, Q. Liu, *Appl. Spectrosc. Rev.*, **50**, No. 5, 387–406 (2015).
38. E. C. Le Ru, L. C. Schroeter, P. G. Etchegoin, *Anal. Chem*., **84**, No. 11, 5074–5079 (2012).
39. B. Negru, M. O. McAnally, H. E. Mayhew, T. W. Ueltschi, L. Peng, E. A. Sprague-Klein, G. C. Schatz, R. P. Van Duyne, *J. Phys. Chem. C*, **121**, No. 48, 27004–27008 (2017).
40. P. Matousek, M. Towrie, C. Ma, W. Kwok, D. Phillips, W. Toner, A. Parker, *J. Raman Spectrosc*., **32**, No. 12, 983–988 (2001).
41. E. W. Van Stryland, M. Sheik-Bahae, In *Characterization Techniques and Tabulations for Organic Nonlinear Optical Materials*, Routledge, 671–708 (2018).
42. M. Sheik-Bahae, A. A. Said, E. W. Van Stryland, *Opt. Lett*., **14**, No. 17, 955–957 (1989).
43. S. Eustis, M. A. El-Sayed, *Chem. Soc. Rev*., **35**, No. 3, 209–217 (2006).
44. L. M. Liz-Marzán, *Langmuir*, **22**, No. 1, 32–41 (2006).
45. N. Sadegh, H. Khadem, S. Tavassoli, *Appl. Opt*., **55**, No. 22, 6125–6129 (2016).
46. D. W. Marquardt, *J. Soc. Ind. Appl. Math*., **11**, No. 2, 431–441 (1963).
47. S. Link, M. A. El-Sayed, *Spectral Properties and Relaxation Dynamics of Surface Plasmon Electronic Oscillations in Gold and Silver Nanodots and Nanorods*, ACS Publ. (1999).
48. M. A. Mahmoud, D. O'Neil, M. A. El-Sayed, *Nano Lett.*, **14**, No. 2, 743–748 (2014).
49. A. De Luca, R. Dhama, A. Rashed, C. Coutant, S. Ravaine, P. Barois, M. Infusino, G. Strangi, *Appl. Phys. Lett*., **104**, No. 10, 103103–103117 (2014).
50. T. Sen, S. Sadhu, A. Patra, *Appl. Phys. Lett.*, **91**, No. 4, 043104–043115 (2007).
51. C. Yun, A. Javier, T. Jennings, M. Fisher, S. Hira, S. Peterson, B. Hopkins, N. Reich, G. Strouse, *J. Am. Chem. Soc.*, **127**, No. 9, 3115–3119 (2005).
52. T. Jennings, M. Singh, G. Strouse, *J. Am. Chem. Soc*., **128**, No. 16, 5462–5467 (2006).
53. A. McLintock, H. J. Lee, A. W. Wark, *Phys. Chem. Chem. Phys*., **15**, No. 43, 18835–18843 (2013).
54. L. Huang, M. Rudolph, F. Rominger, A. S. K. Hashmi, *Angew. Chem. Int. Ed*., **55**, No. 15, 4808–4813 (2016).
55. A. S. K. Hashmi, G. J. Hutchings, *Angew. Chem. Int. Ed.,* **45**, No. 47, 7896–7936 (2006).
56. J. Xie, S. Shi, T. Zhang, N. Mehrkens, M. Rudolph, A. S. K. Hashmi, *Angew. Chem. Int. Ed*., **54**, No. 20, 6046–6050 (2015).